PNAS RESEARCH ARTICLE | CHEMISTRY MEDICAL SCIENCES

pH-degradable, bisphosphonate-loaded nanogels attenuate liver fibrosis by repolarization of M2-type macrophages

Leonard Kaps[a,b], Anne Huppertsberg[c], Niklas Choteschovsky[a], Adrian Klefenz[a], Feyza Durak[d], Babara Schrörs[d], Mustafa Diken[d], Emma Eichler[a], Sebastian Rosigkeit[a], Sascha Schmitt[c], Christian Leps[e], Alicia Schulze[f], Friedrich Foerster[a,b], Ernesto Bockamp[a], Bruno G. De Geest[g], Kaloian Koynov[c], Hans-Joachim Räder[c], Stefan Tenzer[e], Federico Marini[f], Detlef Schuppan[a,h,2], and Lutz Nuhn[c,2]

Edited by Karen Wooley, Texas A&M University, College Station, TX; received December 9, 2021; accepted February 3, 2022

Immune-suppressive (M2-type) macrophages can contribute to the progression of cancer and fibrosis. In chronic liver diseases, M2-type macrophages promote the replacement of functional parenchyma by collagen-rich scar tissue. Here, we aim to prevent liver fibrosis progression by repolarizing liver M2-type macrophages toward a nonfibrotic phenotype by applying a pH-degradable, squaric ester–based nanogel carrier system. This nanotechnology platform enables a selective conjugation of the highly water-soluble bisphosphonate alendronate, a macrophage-repolarizing agent that intrinsically targets bone tissue. The covalent delivery system, however, promotes the drug's safe and efficient delivery to nonparenchymal cells of fibrotic livers after intravenous administration. The bisphosphonate payload does not eliminate but instead reprograms profibrotic M2- toward antifibrotic M1-type macrophages in vitro and potently prevents liver fibrosis progression in vivo, mainly via induction of a fibrolytic phenotype, as demonstrated by transcriptomic and proteomic analyses. Therefore, the alendronate-loaded squaric ester–based nanogels represent an attractive approach for nanotherapeutic interventions in fibrosis and other diseases driven by M2-type macrophages, including cancer.

pH-degradable nanogel | macrophage repolarization | bisphosphonate | drug delivery | fibrosis

Significance

Fibrosis is a consequence of most chronic liver diseases, but currently no approved antifibrotic treatment is available. M2-type macrophages drive fibrosis progression and prevent regression, even when effective causal therapies have been employed. M2-type macrophages activate a cascade of fibrogenic effector cells and can prevent removal of excess scar tissue. To switch these profibrogenic M2 to fibrolytic (regenerative) macrophages, we developed a pH-degradable, nanogel-based delivery system which can be covalently functionalized with the macrophage-repolarizing bisphosphonate alendronate. The nanogels efficiently deliver the clinically approved drug into hepatic nonparenchymal cells after intravenous administration. They do not eliminate macrophages but repolarize their phenotype and subsequently block fibrosis progression. This approach establishes a nanotherapeutic delivery platform to treat further M2-type macrophage-driven diseases, including cancer.

Macrophages are key guardians of the innate system as they fulfill versatile immunological functions ranging from immune defense to balancing of tissue inflammation and repair (1). To carry out these manifold tasks, resident and monocyte-derived macrophages can develop different phenotypes, partly with opposing properties (2). In a simplified perception, macrophages can adopt a proinflammatory M1- or an anti-inflammatory M2-phenotype, which represent two extremes among several other intermediate states. In this paradigm, classical M1 macrophages promote inflammation, immune surveillance, and proteolytic activities including fibrolysis (removal of connective tissue), while M2 macrophages are anti-inflammatory, promote tolerogenic immunity, and support tissue repair by inducing fibrogenesis (deposition of connective tissue), thereby also favoring the development and growth of cancers (3–7). Both extreme phenotypes can be discriminated by specific markers and cytokine profiles. Examples for the M2-polarized macrophages are a high expression of the mannose receptor CD206 (MRC1), the chitinase 3-like 3 protein YM-1, and the immunosuppressive cytokine interleukin (IL)-10, while the M1 macrophages highly express, for instance, the immune stimulatory cytokine tumor necrosis factor α (TNFα) and chemokine (C-C motif) ligand 2 (CCL-2) (8–11). For fibrosis, M2-type macrophages exist in an incomplete form and promote inflammation, as well as fibrogenesis, which emerges once the initial inflammatory triggers subside (12–14). Since M2-polarized macrophages play a key role in fibrosis progression, as well as in cancer, their therapeutic repolarization toward an M1 or elusive regenerative phenotype is a promising concept that has already been confirmed for the therapy of experimental cancers in multiple studies (11, 15, 16).

Liver fibrosis is caused by chronic hepatic inflammation (a wound that does not heal) and frequently develops into cirrhosis (17, 18). It is associated with life-threatening complications including liver failure, infections, portal hypertension with esophageal and variceal bleeding or ascites, and a 2 to 6% annual incidence of primary liver cancer (19). Fibrosis is the excessive accumulation of scar tissue, composed of quantitatively and qualitatively abnormal extracellular matrix (ECM) components and prominently various types of collagen (20), while functional parenchyma decreases (21). The excessive amount of ECM is mostly synthesized by activated, α-smooth muscle actin (α-SMA) positive myofibroblasts, which derive from vitamin A storing hepatic stellate cells or portal/vascular fibroblasts (22). Although considerable progress has been made in the last decades, there is still no approved targeted treatment to reverse or at least

The authors declare no competing interest.

This article is a PNAS Direct Submission.

[1]To whom correspondence may be addressed. Email: detlef.schuppan@unimedizin-mainz.de or lutz.nuhn@mpip-mainz.mpg.de.

This article contains supporting information online at http://www.pnas.org/lookup/suppl/doi:10.1073/pnas.2122310119/-/DCSupplemental.

Published March 15, 2022.

slow down fibrosis progression in the liver, and effective antifibrotic drugs are urgently needed in the clinic (22, 23).

Interestingly, it was recently demonstrated that repurposing of well-established drugs can lead to unexpected therapeutic success. For instance, amphotericin B, originally applied as antifungal drug, can lead to maturation of antigen-presenting cells and was therefore applied as adjuvant during vaccination (24), while disulfiram, originally applied during alcohol abuse to trigger disorders by acetaldehyde dehydrogenase inhibition, gained attention as an antimelanoma drug (25), also in combination with further cancer immunotherapeutics (26). In both cases, a variation of the drug's pharmacokinetic profile was mediated by a macromolecular carrier. Due to their well-established safety record, a repurposing of drugs already approved by the US. Food and Drug Administration seems highly promising, especially with respect to formulating them into nanosized carrier systems.

Bisphosphonates are approved antiresorptive drugs, which are used in clinics for the treatment of osteoporosis and osteolytic metastases (27). Although their entire mechanism of action is not fully understood (28), they are considered to potently inhibit osteoclasts, a specialized bone-resorbing macrophage phenotype (29). This activity has been exploited in studies to demonstrate some therapeutic efficacy in repolarizing tumor-associated M2 macrophages toward tumoricidal M1 macrophages (30–32). However, pharmacokinetics of bisphosphonates to target macrophages outside of bony tissue are extremely poor (33). They exhibit a high affinity to calcium and are rapidly resorbed to bones or otherwise immediately eliminated via the kidneys, especially when applied intravenously (27).

An appealing concept to achieve a high accumulation of bisphosphates for the therapeutic repolarization of profibrotic M2 macrophages in fibrotic livers is the use of a well-defined drug nanocarrier system, which would guide the bisphosphonate drug into the fibrotic organ and effectively into macrophages. Usually, macrophages provide highly phagocytic activity and thus inherently recognize nanosized particles (34). Earlier studies already demonstrated that liposomal formulations, in which bisphosphonates were noncovalently entrapped, could target macrophages—however, not regiospecifically in the liver but systemically followed by complete macrophage depletion (35–37). Unfortunately, these macrophages could still be considered as useful sources for attenuating disease progression, if their phenotype could be reversed, instead of depleting them. Therefore, we designed a nanocarrier system which allows for a covalent conjugation of bisphosphonates, where we hypothesize that the covalent conjugation might also circumvent the bisphosphonate's macrophage depletion but retain its repolarization potential.

One of the clinically well-established bisphosphonates is water-soluble alendronate (AL) (38, 39). Beyond its bisphosphonate motif, it is equipped with a primary amine which can be used for covalent amide coupling to a nanocarrier. Our group has established a core cross-linked micellar nanogel approach derived from reactive precursor block copolymer micelles (40, 41). Upon self-assembly in nonaqueous polar solvents, amine-sensitive reactive ester units inside the micellar cores can be used for covalent drug loading (42–45). However, AL with its primary amine is highly polar and exclusively soluble in water (33). Therefore, nanocarrier ligation needs to be performed in an aqueous solution, making the previous nanogel systems with common amine reactive, but highly hydrolysis-sensitive, activated ester groups [e.g., pentafluorophenyl ester or *N*-hydroxysuccinimide esters (46)] an unattractive choice.

To address this issue, we have established a pH-degradable nanogel carrier system based on hydrolysis-resistant squaric ester groups as amine reactive and selective entities (47). This carrier system can be applied intravenously with prolonged circulation properties (48). In this study, we demonstrate that these so-called squarogels can quantitatively be covalently conjugated with amine-bearing bisphosphonate AL into the nanogel core. After drug functionalization, the resulting AL-loaded nanogel particles (AL/NPs) demonstrate a robust repolarizing effect on M2-type macrophages in vitro and can subsequently be tested in a murine liver fibrosis model with a high abundance of profibrotic M2-type macrophages. AL/NPs induce a strong antifibrotic effect and are well tolerated by the animals, while unconjugated AL is renally cleared and cannot prevent fibrosis progression. Integrated analysis of transcriptomic and proteomic data reveals insight in the mechanism of action and indicates that the antifibrotic effect of AL/NPs is based on the repolarization of profibrotic M2- to antifibrotic M1-type macrophages and thus opens opportunities for nanogel-based immune modulatory treatments of fibrotic livers.

Results and Discussion

To establish bisphosphonate-mediated repolarization of M2- to M1-type macrophages (32, 33, 49) as a therapeutic approach for liver fibrosis, we first aimed to alter their pharmacokinetics (binding to bone and rapid renal excretion) by covalent bisphosphonate ligation to a squaric ester–based, pH-degradable nanogel carrier system.

Synthesis and Characterization of Bisphosphonate-Loaded Nanogel Carrier AL/NPs. As amine-bearing potent bisphosphonate, we selected AL, which has already been clinically approved and applied for decades in the therapy of osteoporosis (39) and bone metastasis (50). Its primary amine group can be exploited under aqueous conditions for the selective and effective conjugation to squaric esters inside the nanogels (Fig. 1*A*). AL can be synthesized readily by a one-pot reaction in a gram scale using phosphorus trichloride and γ-aminobutyric acid in phosphorous acid/methane sulfonic acid (*SI Appendix*, Figs. S1–S4) (38).

The squaric ester–based nanogel carrier system is based on functional amphiphilic block copolymers that self-assemble into polymeric precursor micelles in polar solvents (40, 41). The defined block copolymers are obtained by reversible-addition-fragmentation chain-transfer (RAFT) polymerization of a methacrylamide monomer bearing a functional pendant squaric ester group with a poly(ethylene glycol) (PEG) functionalized macrochain transfer agent (Fig. 1*B*; for details on polymer synthesis and characterization, see *SI Appendix*, Figs. S7–S11 and Table S1). After self-assembly of these defined block copolymers, the hydrophilic PEG shell of the polymeric precursor micelles offers desired stealth properties, while the hydrophobic core with pendant squaric ester groups provides amine reactivity for sequential functionalization (47). Successively, pH-sensitive cross-linking, dye labeling, AL loading, and hydrophilization of the core can be performed through reaction with primary amines (Fig. 1*C*; for details on nanogel fabrication and characterization, see *SI Appendix*, Figs. S12–S25). Stepwise addition of amine-bearing dyes, the acid-degradable bisaminoketal cross-linker 2,2-bis(aminoethoxy)propane, and AL can be followed by UV-vis spectroscopy (*SI Appendix*, Fig. S13).

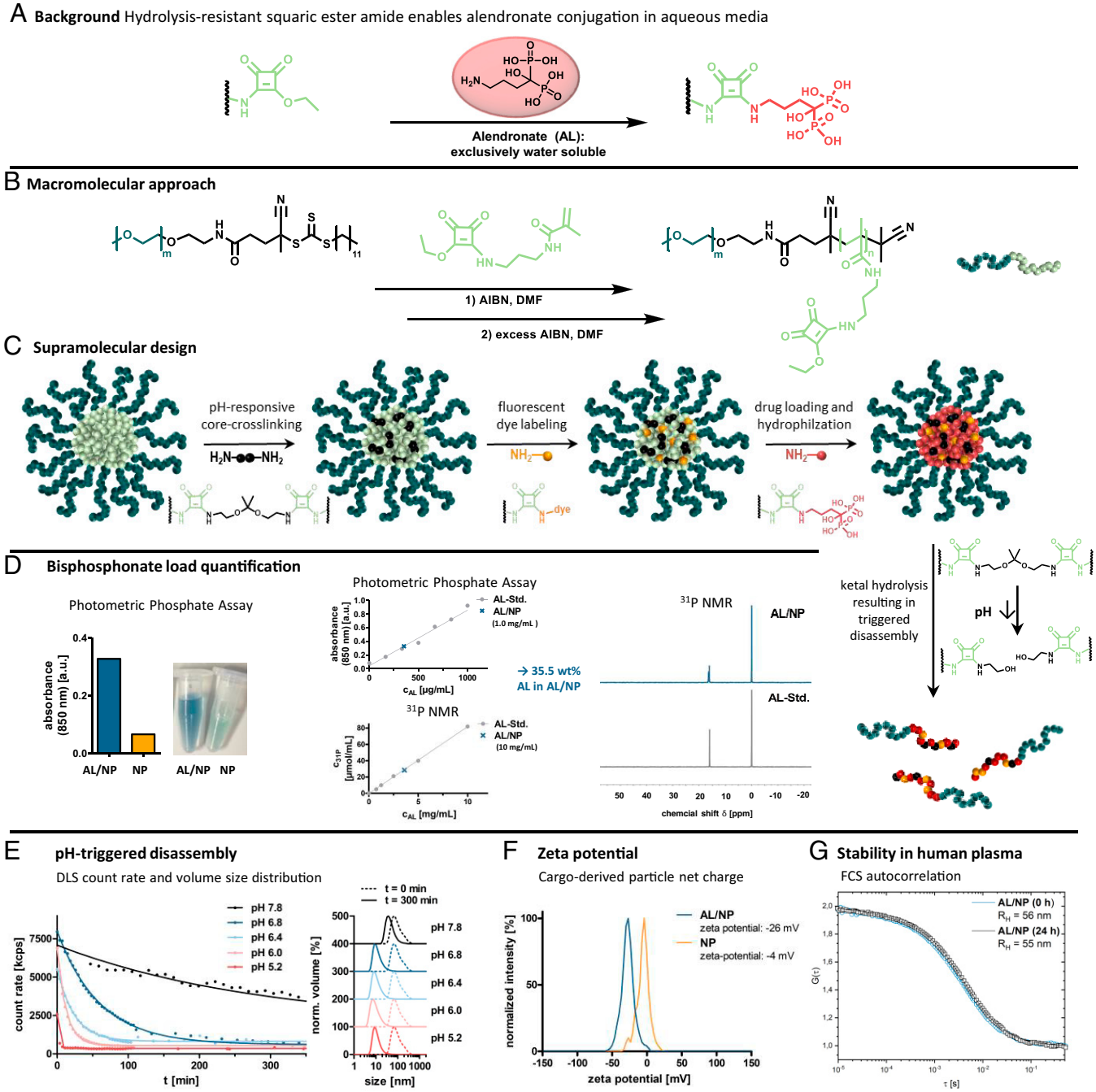

Fig. 1. Nanocarrier fabrication and characterization. (*A*) Background: Covalent AL conjugation can be achieved by squaric ester amides under aqueous conditions. (*B*) Macromolecular approach: Synthesis scheme of RAFT block copolymerization of the squaric ester amide methacrylamide monomer with a PEG-derived chain transfer agent. (*C*) Supramolecular design: Scheme of nanogel fabrication from self-assembled squaric ester amide–based precursor micelles through sequential functionalization, including pH-responsive cross-linking, fluorescent dye labeling, and drug loading. Subsequent pH-triggered degradation can be afforded through acid-promoted hydrolysis of the ketal cross-linkers. (*D*) AL load quantification of AL/NPs using photometric phosphate assay and ^{31}P NMR. (*E*) Ultrasensitive pH-triggered disassembly: DLS count rate of AL/NPs upon exposure to pH 7.8 compared to mildly acidic values of pH 6.8, 6.4, 6.0, and 5.2 over time. DLS size distribution of AL/NPs before (0 min, dotted line), as well as upon, exposure to the different pH values (300 min, solid line). (*F*) Zeta potential of bisphosphonate-loaded AL/NPs compared to control NPs. (*G*) Stability in human plasma: FCS study of AL/NPs after 0 and 24 h of incubation in human blood plasma. R_H, hydrodynamic radii.

Due to the ketal cross-linking (51), the obtained fully hydrophilic AL/NPs degrade upon exposure to mildly acidic endolysosomal pH conditions into single polymer chains. This was demonstrated by dynamic light scattering (DLS) studies showing a decrease in the nanogel's size and count rate upon exposure to physiologically relevant acidic pH values of pH 6.8, 6.4, 6.0, and 5.2. While at the neutral value of pH 7.8 the nanogels remain mostly intact, they already start gradual disassembly at the slightly reduced value of pH 6.8 (found, e.g., in inflamed or tumorous tissue) and fully disintegrate within less than 10 min at pH 5.2 (found intracellularly inside endolysosomes). These results outline a remarkable ultrasensitivity of AL/NPs to subtle pH changes (Fig. 1*E* and *SI Appendix*, Figs. S16 and S17).

The drug load of AL/NPs was quantified by both photometric phosphate assay and ^{31}P NMR spectroscopy (Fig. 1*D*; for details on AL quantification, see *SI Appendix*, Figs. S19–S21). Using external and internal calibration in both methods, the

AL load was determined at 35 wt% for AL/NPs, which is close to the maximum theoretical amount of covalently conjugatable AL per squaric ester group.

For comparative studies, we additionally prepared a reference NP without drug load, where the AL conjugation sites were quenched by a short PEG amine, affording nanogels of similar sizes. However, their zeta potential was determined as almost neutral (−4 mV), while the bisphosphonate-loaded AL/NPs provided a negative zeta potential of −26 mV (Fig. 1*F* and *SI Appendix*, Fig. S15), confirming the covalent conjugation of the negatively charged phosphonate groups of AL.

Prior to all in vitro and in vivo studies, the AL/NPs' stability in blood plasma as a biologically relevant medium was investigated by fluorescence correlation spectroscopy (FCS). This technique provides information about the size of fluorescently labeled nanocarriers in solution or even complex media such as blood plasma. By this means, potential aggregation or degradation of nanocarriers would be revealed by an increase or decrease in the nanocarrier's size. For these measurements, fluorescent Oregon green–labeled AL/NPs (OG-AL/NPs) were incubated in blood plasma for 0 or 24 h. From subsequent FCS measurements, it was evident that the recorded autocorrelation curves and the resulting hydrodynamic radii remained unchanged (Fig. 1*G* and *SI Appendix*, Fig. S23). Thus, neither aggregation nor degradation of the nanocarriers resulted from exposure to plasma components. Additionally, we confirmed its inert behavior by multiangle DLS measurements of unlabeled nanogels in plasma (*SI Appendix*, Fig. S22). By applying a multicomponent analysis (52), no aggregation was found underlining the profound stability of the AL/NP nanocarrier in complex biological media. This behavior is an important prerequisite for safe intravenous administration of nanoparticles.

Biocompatible AL/NPs Repolarize Profibrotic M2-Type toward Antifibrotic M1-Type Macrophages In Vitro. Next, we assessed the in vitro cytotoxicity of AL/NPs in native (M0) and polarized M1- and M2-type RAW macrophages, mirroring characteristics of primary murine macrophages (*SI Appendix*, Fig. S26). Minor cytotoxicity was primarily related to the bisphosphonate, not to the carrier itself, as no increased toxicity of nanoparticle-conjugated AL compared to free AL was observed. Afterward, we tested the in vitro cellular uptake of AL/NPs and the corresponding unloaded carrier NP in M2-polarized primary macrophages from bone marrow, which resemble murine liver macrophages in their M2 stage. OG-AL/NP and Oregon green control NP (OG-NP) were incubated for 24 h and then analyzed by flow cytometry. OG-AL/NP was dose-dependently taken up, while the carrier OG-NP alone showed only minor uptake (Fig. 2 *A* and *B* and *SI Appendix*, Fig. S25). This was further confirmed by fluorescence microscopy studies where a strong Oregon green (OG)–related fluorescence was observed for OG-AL/NP inside the M2 macrophages at increasing doses, while it was nearly absent for OG-NP at the highest dose (Fig. 2*C*). We hypothesize that this preferential M2 uptake might correlate with the enhanced expression levels of scavenger receptors on M2 macrophages that mediate the uptake of negatively charged macromolecules (53–55).

Next, we investigated the in vitro repolarization effect of NP-conjugated AL versus soluble AL on M2-polarized primary macrophages toward a M1-phenotype. At high and low doses (30 and 60 μM AL), AL/NPs significantly ($P < 0.001$) reduced typical M2-phenotype markers YM-1 and IL-10 on the transcript level (Fig. 2*D*), which could be confirmed on the protein level for IL-10 by flow cytometric analysis (Fig. 2 *E* and *F*). This was also the case for soluble AL at high dose. Besides down-regulation of M2-phenotypic markers, we also assessed the up-regulation of M1-phenotype markers. Here, CCL-2 was significantly ($P < 0.05$) up-regulated at a high dose exclusively for the AL/NP-treated primary macrophages, in contrast to soluble AL. Further, AL/NP treatment, but not soluble AL treatment, significantly stimulated the secretion of TNFα, another M1-phenotype–related cytokine, in M2-polarized primary macrophages as determined by enzyme-linked immunosorbent assay (ELISA) (Fig. 2*G*). This was again enhanced for the nanogel-conjugated sample compared to the free drug, corroborating a nanogel-mediated benefit on bisphosphonate delivery already in cell culture.

Nanogels Guide AL Delivery to (Non)parenchymal Liver Cells of Mice with Liver Fibrosis. The biodistribution of AL/NPs was investigated in both healthy and liver fibrotic mice, since pharmacokinetics can differ in fibrotic animals, as shown by us previously (Fig. 3*A* and *SI Appendix*, Fig. S28) (56). Mice with parenchymal liver fibrosis due to treatment with escalating doses of oral CCl_4 represent a reproducible and progressive model of parenchymal liver fibrosis (57). They mimic fibrosis development in alcoholic and to some degree also nonalcoholic steatohepatitis or viral liver fibrosis, which represent by far the most frequent etiologies of end-stage liver disease worldwide (21). Moreover, progression of these chronic liver diseases is driven and perpetuated by the M2-polarized macrophages. This pathogenic feature can also be observed in CCl_4-induced fibrotic livers, as exemplified by high collagen content that is accompanied by increased expression of the M2 macrophage marker CD206 (Fig. 3 *B* and *C*).

Mice treated with CCl_4 three times a week over 5 wk (Fig. 3*A*) developed reproducible and advanced liver fibroses compared to their controls treated with mineral oil as vehicle (Fig. 3*C*) (7, 57–59). Healthy and fibrotic mice received a single intravenous dose of near-infrared (NIR) dye 800RS-labeled AL/NPs (NIR-AL/NPs) or AL-free control particles (NIR-NPs). Moreover, we also prepared and applied a nanogel-free 800RS-AL conjugate representing the free drug (NIR-AL; compare *SI Appendix*, Figs. S5 and S6). Directly after intravenous injection, the body distribution was monitored using the 800RS-derived NIR fluorescence monitored by an in vivo NIR-imaging system (Fig. 3*D*). Instantly after injection, the unloaded carrier NIR-NPs showed no distinct organ tropism, and their fluorescence signal was distributed over the thorax and abdomen of the mice, reflecting the carriers' prolonged circulation in the blood stream, as reported earlier (47). In contrast, the free-drug NIR-AL alone generated modest hepatic fluorescence, which rapidly faded and was nearly absent at 48 h, likely due to renal excretion (Fig. 3*D*). Interestingly, NIR-AL/NPs were rapidly sequestrated in the livers and remained in the organs at high signal intensities over the following 48 h (Fig. 3*D*). 48 h after injection, mice were killed, and their organs were dissected for ex vivo imaging (Fig. 3*E*). In line with the previous observations in vivo, NIR-AL/NPs were prominently localized ex vivo in the livers, and only low hepatic fluorescence signals were detected for NIR-AL and NIR-NPs (Fig. 3*F*).

Next, we studied cell-specific NP uptake in vivo after digestion of the isolated livers. The resulting single-cell suspension was subjected to flow cytometrical analysis (Fig. 3*G* and *SI Appendix*, Fig. S29 for corresponding gating strategies). While little uptake was found for the empty control nanogels with NP, the nanogels with NIR-AL/NP were efficiently engulfed by nonparenchymal cells, including macrophages and endothelial and dendritic cells. This uptake was significantly higher than for unconjugated NIR-AL. For parenchymal cells

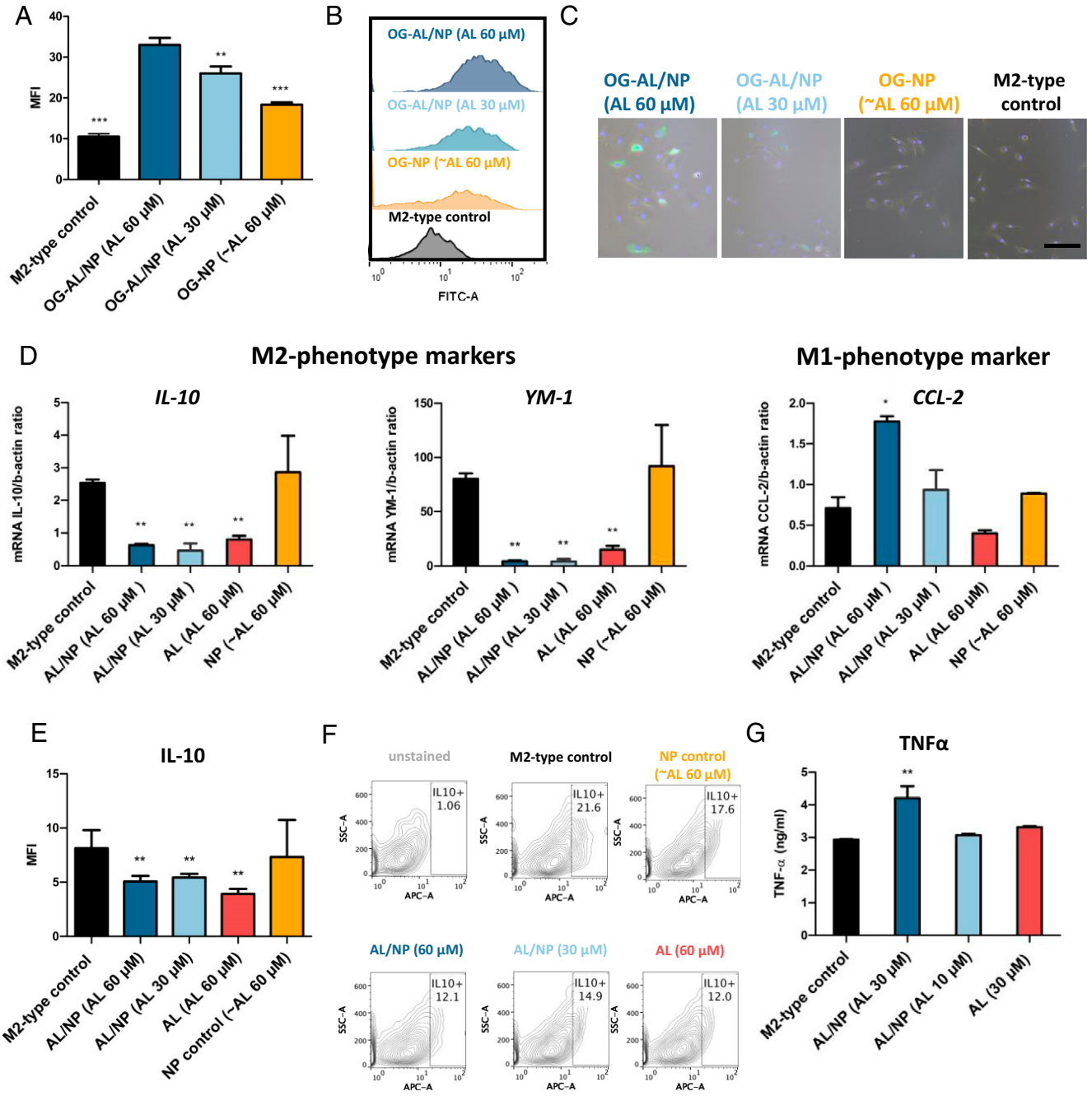

Fig. 2. In vitro performance of AL/NPs. (*A*) In vitro cellular uptake by mean fluorescence intensity (MFI) of OG-AL/NPs (30 and 60 µM AL) and control particle OG-NPs (at a representative concentration of ~60 µM AL) in M2-polarized primary macrophages (incubation time of 24 h, $n = 3$, $^{**}P < 0.001$, $^{***}P < 0.0001$, OG-AL/NPs vs. control). (*B*) Histograms of representative samples of *A*. (*C*) In vitro brightfield fluorescence microscopy of M2-polarized primary macrophages incubated with OG-AL/NPs (30 and 60 µM AL), OG-NPs, and untreated M2 macrophages as control (incubation time, 24 h). (Scale bar, 100 µm.) (*D*) AL/NP treatment significantly reduces the transcript levels of the M2-phenotype markers *IL-10* and *YM-1*, while the M1-phenotype marker *CCL2* was increased as determined by qPCR (incubation time, 48 h; $n = 3$; $^{*}P < 0.05$, $^{**}P < 0.001$ vs. M2-type control). (*E*) AL/NP (30 and 60 µM AL) treatment significantly reduced IL-10 protein expression in M2-type primary macrophages as determined by flow cytometry (incubation time of 48 h, $n = 3$, $^{**}P < 0.001$). (*F*) Contour plots of representative samples of *E*. (*G*) Quantification of TNFα protein levels in supernatants collected from M2-type macrophages treated with AL/NPs (30 and 10 µM AL) and controls (30 µM soluble AL or untreated) as determined by ELISA (incubation time of 48 h, $n = 3$, $^{**}P < 0.001$).

(hepatocytes), only little signals were found for all three species. Despite NIR-AL/NP's large accumulation in the liver, its absence from parenchymal cells can explain the excellent biocompatibility and absent toxicity of our nanogels (6, 7, 58, 59). In line with this assumption, we found no acute in vivo toxicity comparing AL/NP-treated mice and controls. Apart from no visible damage to major organs like lungs, kidneys, and intestine (the weights of liver and spleen were also not affected after multiple treatments; *SI Appendix*, Fig. S30), normal safety blood parameters indicated the absence of hemolysis (lactate dehydrogenase), liver injury or inflammation (aspartate transaminase or alanine transaminase), and renal (urea or creatinine) toxicity (*SI Appendix*, Fig. S31). Note that biodistribution in healthy mice did not differ from that in fibrotic mice (*SI Appendix*, Fig. S28). Again, NIR-AL/NPs were rapidly sequestrated in the liver and efficiently taken up by nonparenchymal cells, underlining the nanocarriers' safety profile.

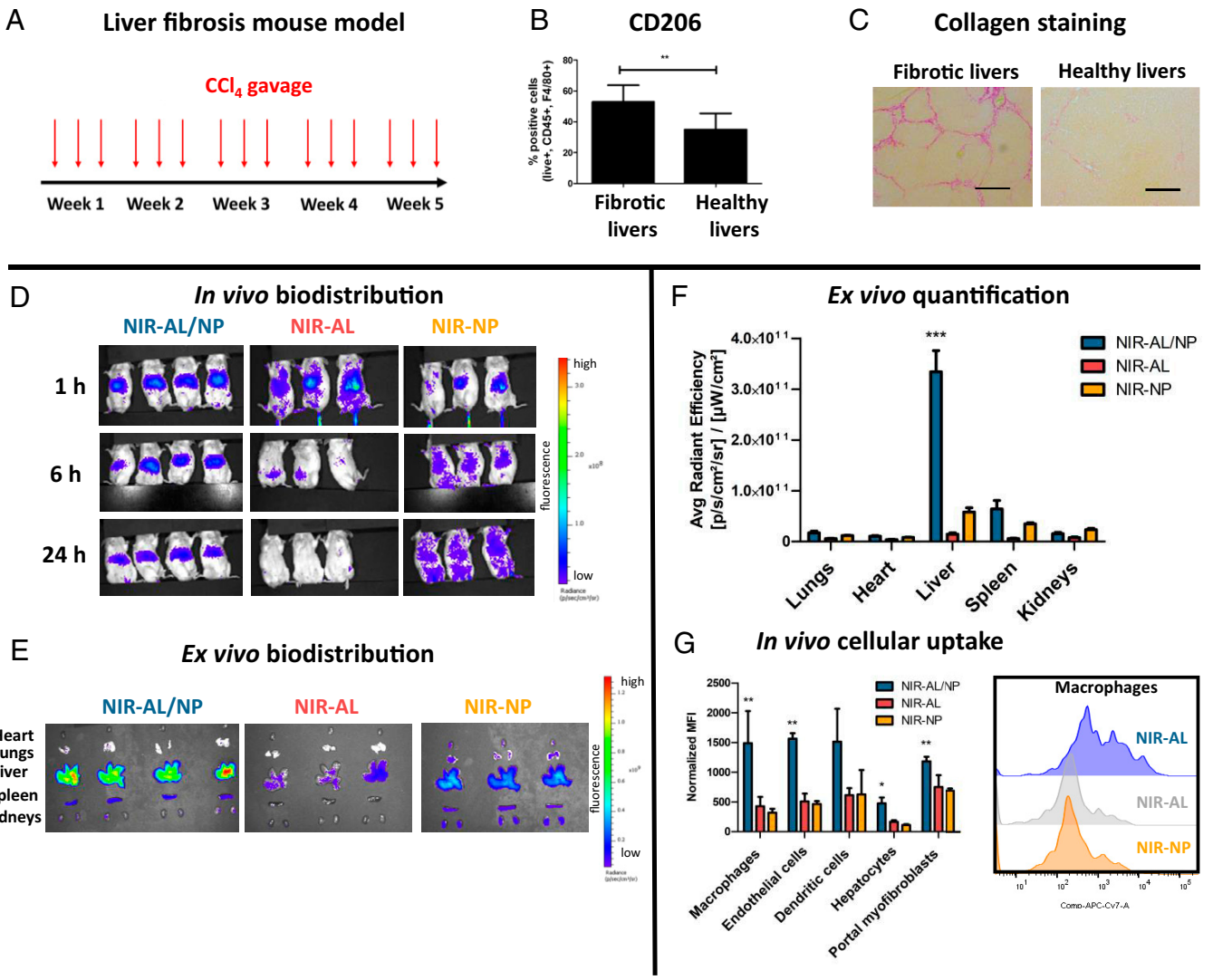

Fig. 3. Biodistribution of NIR-AL/NPs in livers of CCl_4 fibrotic mice. (*A*) CCl_4 liver fibrosis mouse model. Mice were gavaged with increasing doses of CCl_4 three times weekly over 5 wk. (*B*) Frequency of M2-polarized macrophages in fibrotic and healthy livers as determined from single-cell suspension of digested livers by flow cytometry (**$P < 0.001$). (*C*) Representative liver sections stained with Sirius red to visualize collagen. (Scale bars, 100 µm.) (*D*) In vivo biodistribution of NIR-AL/NPs. CCl_4 fibrotic mice were intravenously injected with NIR-AL/NPs (4 mg/kg AL) or controls (NIR-AL and NIR-NPs), and biodistribution was monitored by NIR imaging at 1, 6, and 24 h. (*E*) Ex vivo imaging of extracted organs after 24 h. (*F*) Quantification of organ fluorescence by average radiant efficiency of the extracted organs shown in *E* (***$P < 0.0001$). (*G*) In vivo cellular uptake of NIR-AL/NPs and controls in liver cells, as quantified by flow cytometry of liver single-cell suspension obtained from livers shown in *E*, and corresponding representative histograms of the cellular uptake of NIR-AL/NPs and controls in liver macrophages (*$P < 0.05$, **$P < 0.001$).

AL-Loaded Nanogels Induced a Robust Antifibrotic Effect in CCl_4 Liver Fibrotic Mice. To evaluate the antifibrotic effect of AL/NPs, mice were gavaged with CCl_4 as described before (Fig. 3*A*). At the beginning of week 4, fibrotic mice received a total of six injections of AL/NPs (4 or 2 mg/kg AL) over 2 wk (Fig. 4*A*). Equivalent doses of nonloaded nanogels NPs, as well as nonconjugated, soluble AL, served again as control. After 24 h of the last treatment, mice were killed and livers were extracted to evaluate the fibrosis-related biomarker hydroxyproline (HYP), a posttranslationally modified amino acid that is almost exclusively present in collagenous proteins as the main ECM components of fibrosis (for liver and spleen weights at kill time, see *SI Appendix*, Fig. S30) (58–61). Hepatic collagen accumulation was strongly and dose-dependently suppressed up to 80% by AL/NP treatment, while unconjugated AL and empty NPs had no significant antifibrotic effect (Fig. 4*B*). Notably, despite the late-onset treatment, AL/NPs normalized liver collagen down to reference levels of healthy control mice (receiving mineral oil without CCl_4). These results show comparable antifibrotic efficacy to nanogels loaded with small interfering RNA (siRNA) targeting *COL1A1*, which encodes the most prevalent collagen in fibrosis (58, 59). As the squaric ester amide–based control nanogel carrier NP alone had no antifibrotic effect and the unconjugated AL effects were only minor, we concluded that a conjugation of AL to the nanogel carrier AL/NP improves the pharmacokinetics and hypothesized that a M2- to M1-phenotype repolarization of macrophages in the fibrotic tissue is involved which attenuates liver fibrosis (Fig. 4*B*).

Further, tissue sections from left and middle liver lobes were assessed for morphometric collagen deposition by Sirius red staining, as depicted in Fig. 4*C*. Morphometric collagen quantification represents a more accurate method to determine pathologically relevant collagen, as larger vessels and portal areas are omitted which are naturally rich in collagen (58, 59, 62). Indeed, this fibrosis assessment more clearly confirmed that

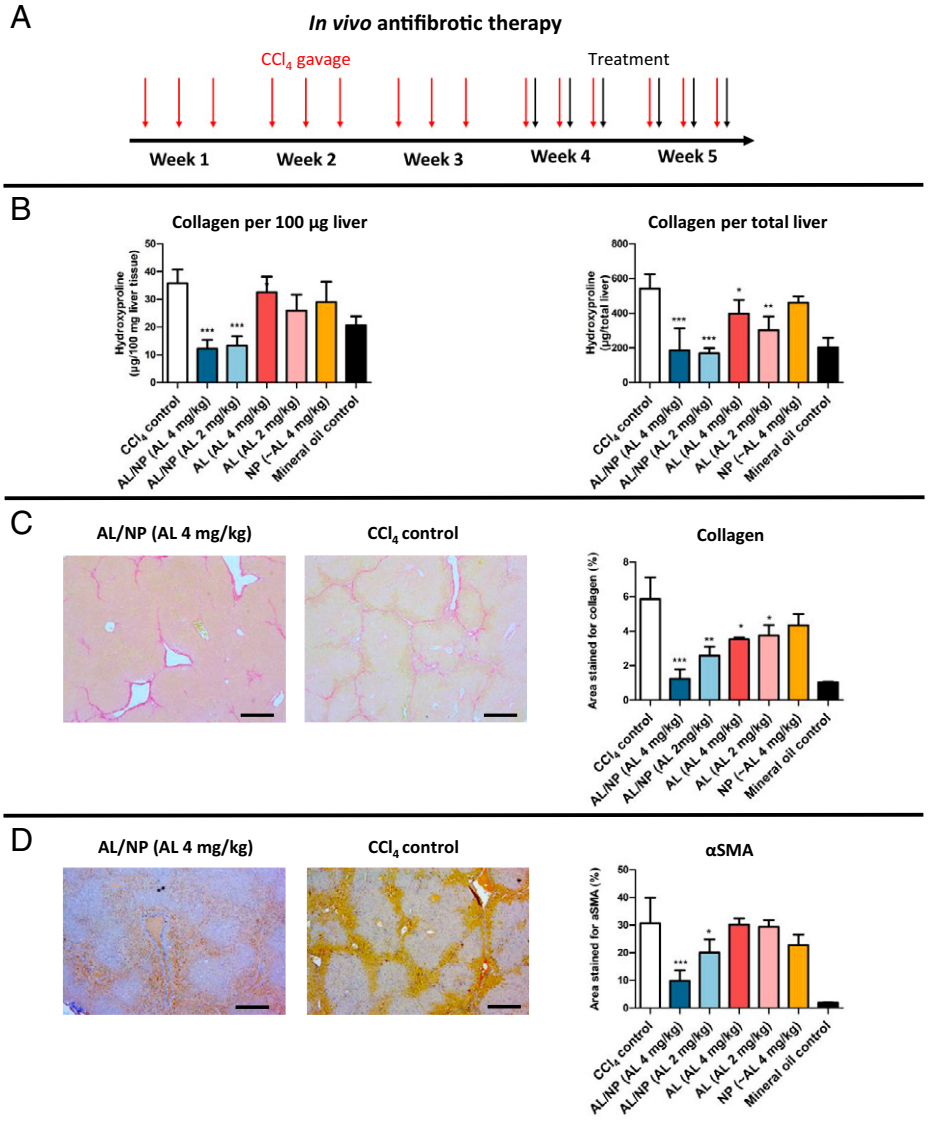

Fig. 4. In vivo antifibrotic effect of AL/NPs in CCl_4 fibrotic mice. (*A*) Treatment schedule for mice that were gavaged with CCl_4 three times a week for 5 wk. During the last 2 wk, mice received six intravenous injections of AL/NPs (2 or 4 mg/kg AL) or corresponding controls (unconjugated 2 or 4 mg/kg AL and NPs). 24 h after the final injection, mice were killed and livers were analyzed. (*B*) Collagen quantified by relative or total liver HYP content. (*C*) Morphometric assessment of collagen deposition in representative Sirius red–stained liver tissue sections (five randomly selected fields of each specimen omitting large vascular structures). (Scale bars, 200 µm.) (*D*) Morphometric assessment of α-SMA+ myofibroblasts in representative liver sections (means ± SD; $*P < 0.05$, $**P < 0.001$, $***P < 0.0001$ vs. CCl_4 fibrotic control mice; $n = 5$–7 in the treatment and CCl_4 fibrotic control groups, $n = 4$ in the mineral oil control group). (Scale bars, 200 µm.)

AL/NPs strongly reduced the regiospecific collagen load in contrast to unconjugated AL (Fig. 4*C*). In complete accordance, α-SMA–positive cells that represent activated myofibroblasts as the main collagen source during fibrosis were also significantly and dose-dependently suppressed in the AL/NP-treated groups, corroborating the antifibrotic effect of AL/NPs (Fig. 4*D*).

AL/NP Treatment Shifts the Fibrotic Liver Immunome toward a Proinflammatory and Immunocompetent State. Transcriptomic and proteomic experiments were performed to gain mechanistic insight into the AL/NP-mediated antifibrotic effect. First, comparative high-throughput RNA sequencing (RNA-seq) was performed on representative liver samples of AL/NP- vs. CCl_4-treated mice (each $n = 3$) to reveal differences on the transcriptional level between the two groups. Differential gene expression analysis revealed 108 down-regulated genes and 144 up-regulated genes between treated vs. untreated fibrotic control mice, as visualized by the volcano plot (Fig. 5*A*; $\log_2$-fold change ≥ 1 or ≤ -1, false discovery rate [FDR] < 0.05).

In principal component analysis, a method to describe similarities and variances between groups (63), AL/NP treatment induced a transcriptional phenotype distinctly different from fibrotic control mice and with a defined clustering between the groups (Fig. 5*B*).

Looking at the top up-regulated inflammatory genes, all of them (e.g., *SAA*, *IL-1*, *CD11b*, and *CRP*) are involved in proinflammatory immune responses (Fig. 5*C*, *Top*), while several of the top down-regulated inflammatory genes (e.g., *FMO3*, *ABCG5/8*, and *MAP2K6*) are otherwise involved in anti-inflammatory immune responses (Fig. 5*C*, *Bottom*). Ingenuity pathway analysis (IPA) was performed to correlate immunological fibrosis-associated pathways with the effective nanogel-mediated bisphosphonate treatment (64). IPA takes the related differential gene expression levels with activation and deactivation of relevant signaling pathways into account. For instance,

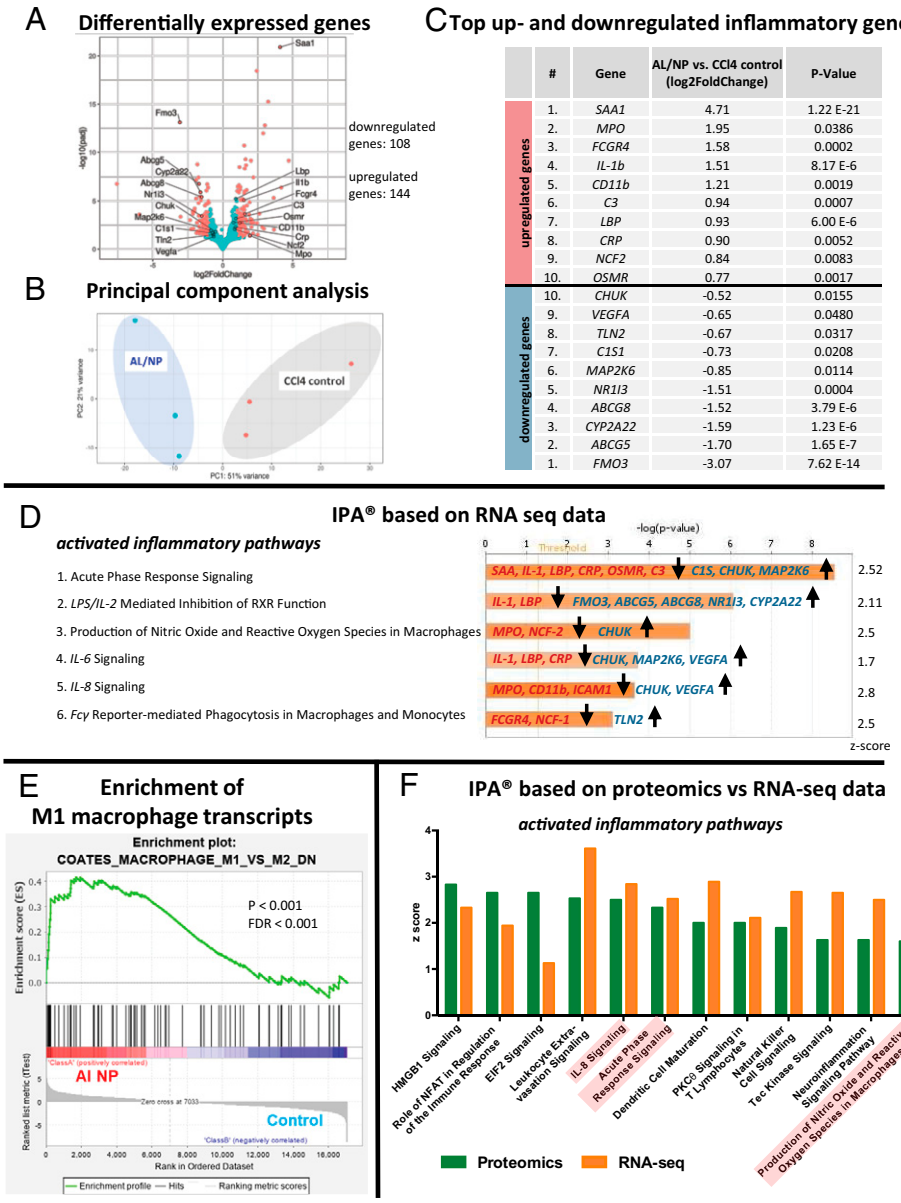

Fig. 5. Comparative transcriptomic and proteomic analyses by high-throughput RNA-seq (supported by mass spectrometry proteomics) of representative liver samples from AL/NP-treated (4 mg/kg AL) vs. untreated CCl_4 fibrotic livers (each $n = 3$). (*A*) Volcano plot and numbers of significantly differentially expressed genes between AL/NP-treated and fibrotic mice. Differentially expressed genes with $\log_2$-fold change ≥ 1 or ≤ -1 and FDR ≤ 0.05 are shown in red, and the top 10 up- and down-regulated inflammatory genes are labeled. (*B*) Principal component (PC) analysis based on RNA-seq data indicates clustering of AL/NP-treated vs. CCl_4 control mice (PC1 51% and PC2 21% variance, respectively). (*C*) Top 10 up- and down-regulated genes associated with inflammation as determined by RNA-seq (padj, *P* values adjusted for multiple testing by the Benjamini-Hochberg method). (*D*) Relevant immune-related signaling pathways, which were found to be activated as predicted by IPA based on RNA-seq differential expression data (bars represent *P* values adjusted for multiple testing by the Benjamini-Hochberg method, the yellow line indicates the ratio of molecules which are regulated in a given pathway and meet the cutoff criteria, and the involved up- and down-regulated genes are mentioned). (*E*) GSEA of differentially expressed genes in AL/NP-treated livers, compared with CCl_4 fibrotic control livers, identified highly enriched genes in gene sets related to M1- vs. M2-type macrophages ($P < 0.001$, FDR < 0.001). (*F*) Comparative IPAs of activated inflammatory pathways for RNA-seq vs. proteomics data obtained from quantitative proteomic analysis by mass spectrometry (the three most significant pathways identified by RNA-seq IPAs are highlighted in red). Proteomic analysis supported the previous transcriptomic results, corroborating that macrophage-repolarizing inflammatory pathways are activated by AL/NP treatment.

serum amyloids (SAAs) are located downstream in the acute phase response signaling pathway (Fig. 5*D*, pathway 1) and were found to be highly up-regulated (e.g., *SAA*, $\log_2$-fold change of 4.7) in our dataset (Fig. 5*B*) and thus confirm the predicted activation of the acute phase response signaling pathway by IPA (the related acute phase response signaling pathway is shown in *SI Appendix*, Fig. S33). In analogy, other relevant proinflammatory pathways were identified by this method, too (e.g., lipopolysaccharide (LPS)/ IL-2 mediated inhibition of retinoid X receptor (RXR) function, production of nitric oxide and reactive oxygen species in macrophages, and IL-6 and IL-8 signaling). Beyond IPA, RNA-seq data were also analyzed by gene set enrichment analysis (GSEA), which represents another powerful analytical method to interpret large gene expression data by focusing on gene sets rather than single genes (65). GSEA finally demonstrated significant enrichment in gene sets related to M1-type macrophage polarization and down-regulation of M2-type phenotypes in AL/NP-treated versus fibrotic control mice (Fig. 5*E*).

Moreover, we aimed to corroborate the obtained results of the RNA-seq analyses by performing quantitative proteomic analyses via mass spectrometry of the same samples (*SI Appendix*, Fig. S34).

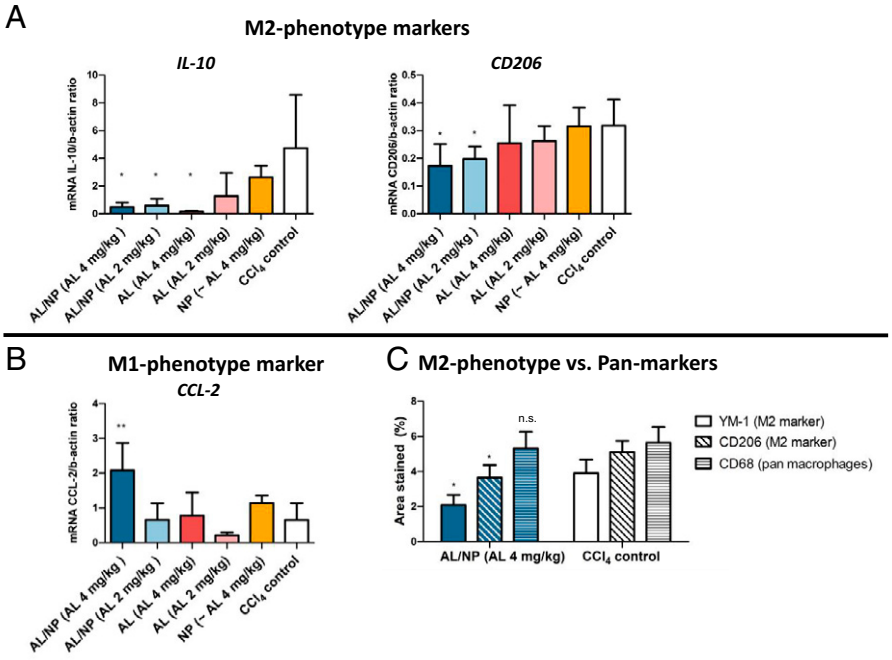

Fig. 6. Repolarization of M2 to M1 macrophage–phenotype markers by AL/NP treatment. (*A* and *B*) AL/NP treatment significantly reduced the M2-phenotype markers *IL-10* and *CD206* (*A*), while the M1-phenotype maker *CCL2* was up-regulated (*B*) on the transcriptome as determined by qPCR (*$P < 0.05$,**$P < 0.001$). (*C*) In liver sections stained for the pan-macrophage marker CD68 or the M2 markers YM-1 and CD206, AL/NP treatment significantly reduced the M2-type markers YM-1 and CD206 on the protein level, while CD68 was not affected (*$P < 0.05$; n.s., not significant).

The results of the proteomic data were compared to RNA-seq data using IPA as a statistical tool, confirming similar activation of relevant pathways in good agreement with the RNA-seq data (Fig. 5*F*). Due to limits in proteome coverage, not all pathways identified by RNA-seq could be confirmed on the proteome level. Nonetheless, the combined transcriptomic and proteomic results suggest that AL/NPs' contributions to a fibrolytic state are triggered by a switch toward proinflammatory and immunocompetent behavior.

AL/NP Treatment Repolarizes Profibrotic M2 Macrophages to Fibrolytic M1 Macrophages In Vivo. To confirm effective M2 macrophage repolarization in vivo, we combined our in vitro repolarization results with the transcriptome data from our in vivo experiments of AL/NP treatment vs. no treatment in CCl_4 fibrotic livers. Based on experimental data curated by IPA, we analyzed how far the deregulated genes have an immunomodulatory effect on the activation or deactivation of the M1- or M2-related targets. During these analyses, IPA predicts that the up-regulated proinflammatory genes (e.g., *IL-1*, *SAA*, and *C3*) of the dataset would also induce M1-phenotype markers (*IL-6*, *INFγ*, *CCL2*, and *SOCS3*), while M2-type markers (*Arg1*, *CD206*, and *IL-10*) would be down-regulated (*SI Appendix*, Fig. S33). To further confirm this assumption, we found down-regulation of the M2-phenotype markers *YM-1*, *CD206*, and *IL-10* (Fig. 6 *A* and *C*) and up-regulation of the M1-type marker *CCL2* (Fig. 6*B*) in the AL/NP-treated vs. all other groups on both the transcript and the protein expression levels, while the overall macrophage count, which can be affected, e.g., by the liposomal bisphosphonate treatment clodronate (66), remained unchanged (Fig. 6*C* and *SI Appendix*, Fig. S32). Therefore, only the macrophages' repolarization led to the exclusive fibrolytic outcome for the AL/NP-treated mice and underlines the opportunity that the squaric ester-based nanogels guarantee a focused delivery of AL to profibrotic hepatic M2-type macrophages in order to attenuate liver fibrosis.

Conclusion

In this study, we applied a squaric ester–based nanogel carrier system for covalent conjugation of the exclusively water-soluble bisphosphonate AL. This macromolecular delivery approach enabled efficient AL delivery to hepatic macrophages (and other nonparenchymal cells), resulting in a highly effective treatment of experimental liver fibrosis after intravenous administration.

While the hydrophilic AL-loaded nanogels provided high stability in blood plasma for up to 24 h, their engineered pH-programmed degradability upon exposure to slightly acidic endolysomal pH values renders their high biocompatibility. We first demonstrated their potential to not eliminate but reprogram profibrotic M2- toward antifibrotic M1-phenotype macrophages in vitro on the transcriptomic and protein levels. In vivo, the nanogel carrier modified AL's biodistribution, resulting in strong accumulation in the liver and prominent uptake in relevant nonparenchymal liver cells, including profibrotic M2 macrophages as key contributors to fibrosis progression. This resulted in a marked antifibrotic effect for fibrotic mice treated with AL/NPs, whereas free AL and control NP alone were ineffective. Further insights into the therapeutic effect were gained by transcriptomic and proteomic analyses. Multiparameter data assessment of AL/NP-treated vs. untreated fibrotic livers identified multiple regulated genes, proteins, and pathways involved in proinflammatory macrophage polarization, supporting a M2- to M1-phenotype switch of hepatic macrophages, which was further corroborated by tissue analysis revealing no macrophage depletion but repolarization.

These findings emphasize the virtue of our nanogel carriers as a biocompatible nanocarrier platform to treat liver diseases, as exemplified by effective hepatic delivery of AL that would otherwise bypass the fibrotic liver. Moreover, the nanocarriers' prominent targeting of nonparenchymal cells, including profibrotic macrophages and subsequent phenotype repolarization, attenuates liver fibrosis. Consequently, this nanogel platform presents an attractive tool for further interventions in M2-phenotype

macrophage-dominated diseases. This may include combinatorial approaches against cancer where the presence of M2-type macrophages still correlates with reduced efficacy of current state-of-the-art cancer immunotherapeutics. Thereby, not only intravenous injection routes but also local injection into the diseased site (e.g., tumor) could be exploited as a promising route to maximize AL delivery.

Data Availability. All study data are included in the article and/or *SI Appendix*.

ACKNOWLEDGMENTS. The authors' work was gratefully supported by the German Research Foundation through the Collaborative Research Center/Sonderforschungsbereich (CRC/SFB) 1066 (projects B03, B04, B17, Q02, Q04, and Q06) as well as the Emmy Noether program to L.N. Christine Rosenauer is acknowledged for DLS studies in blood plasma. Moreover, A.H. and L.N. acknowledge the Max Planck Graduate Center with the Johannes Gutenberg-University Mainz, as well as Tanja Weil for providing access to excellent laboratory facilities. L.K. acknowledges support by the CRC/SFB 1066 steering committee for approving a starter grant to perform the transcriptomic analyses, which have further been supported by the computing infrastructure provided by the Core Facility Bioinformatics at the University Medical Center, Johannes Gutenberg-University Mainz. Dorothe Thies is acknowledged for her assistance during the cell culture work and analytical readouts.

Author affiliations: [a]Institute of Translational Immunology and Research Center for Immune Therapy, University Medical Center, Johannes Gutenberg-University Mainz, 55131 Mainz, Germany; [b]Department of Internal Medicine I, University Medical Center, Johannes Gutenberg-University Mainz, 55131 Mainz, Germany; [c]Max Planck Institute for Polymer Research, 55128 Mainz, Germany; [d]TRON-Translational Oncology gGmbH, University Medical Center, Johannes Gutenberg-University Mainz, 55131 Mainz, Germany; [e]Institute for Immunology, University Medical Center, Johannes Gutenberg-University Mainz, 55131 Mainz, Germany; [f]Institute of Medical Biostatistics, Epidemiology and Informatics, University Medical Center, Johannes Gutenberg-University Mainz, 55131 Mainz, Germany; [g]Department of Pharmaceutics and Cancer Research Institute Ghent, Ghent University, 9000 Ghent, Belgium; and [h]Division of Gastroenterology, Beth Israel Deaconess Medical Center, Harvard Medical School, Boston, MA 02215

Author contributions: L.K., A.H., D.S., and L.N. designed research; L.K., A.H., N.C. (part of the data will be used in his medical doctoral thesis), A.K., F.D., S.R., S.S., C.L., F.F., F.M., and L.N. performed research; B.S., M.D., E.E., S.R., A.S., E.B., B.G.D.G., K.K., H.-J.R., and S.T. contributed new reagents/analytic tools; L.K., A.H., B.S., F.M., D.S., and L.N. analyzed data; and L.K., A.H., D.S., and L.N. wrote the paper.

1. O. Krenkel, F. Tacke, Liver macrophages in tissue homeostasis and disease. *Nat. Rev. Immunol.* **17**, 306–321 (2017).
2. K. Liddiard, P. R. Taylor, Understanding local macrophage phenotypes in disease: Shape-shifting macrophages. *Nat. Med.* **21**, 119–120 (2015).
3. P. J. Murray *et al.*, Macrophage activation and polarization: Nomenclature and experimental guidelines. *Immunity* **41**, 14–20 (2014).
4. C. Yunna, H. Mengru, W. Lei, C. Weidong, Macrophage M1/M2 polarization. *Eur. J. Pharmacol.* **877**, 173090 (2020).
5. L. Kaps, D. Schuppan, Targeting cancer associated fibroblasts in liver fibrosis and liver cancer using nanocarriers. *Cells* **9**, 2027 (2020).
6. N. Leber *et al.*, α-mannosyl-functionalized cationic nanohydrogel particles for targeted gene knockdown in immunosuppressive macrophages. *Macromol. Biosci.* **19**, e1900162 (2019).
7. L. Kaps *et al.*, In vivo siRNA delivery to immunosuppressive liver macrophages by α-mannosyl-functionalized cationic nanohydrogel particles. *Cells* **9**, 1905 (2020).
8. E. Van Overmeire *et al.*, M-CSF and GM-CSF receptor signaling differentially regulate monocyte maturation and macrophage polarization in the tumor microenvironment. *Cancer Res.* **76**, 35–42 (2016).
9. K. Movahedi *et al.*, Different tumor microenvironments contain functionally distinct subsets of macrophages derived from Ly6C(high) monocytes. *Cancer Res.* **70**, 5728–5739 (2010).
10. K. A. Jablonski *et al.*, Novel markers to delineate murine M1 and M2 macrophages. *PLoS One* **10**, e0145342 (2015).
11. E. Bolli *et al.*, Targeted repolarization of tumor-associated macrophages via imidazoquinoline-linked nanobodies. *Adv. Sci. (Weinh.)* **8**, 2004574 (2021).
12. S. Y. Weng *et al.*, IL-4 receptor alpha signaling through macrophages differentially regulates liver fibrosis progression and reversal. *EBioMedicine* **29**, 92–103 (2018).
13. P. Ramachandran *et al.*, Differential Ly-6C expression identifies the recruited macrophage phenotype, which orchestrates the regression of murine liver fibrosis. *Proc. Natl. Acad. Sci. U.S.A.* **109**, E3186–E3195 (2012).
14. K. Kazankov *et al.*, The role of macrophages in nonalcoholic fatty liver disease and nonalcoholic steatohepatitis. *Nat. Rev. Gastroenterol. Hepatol.* **16**, 145–159 (2018).
15. Z. Duan, Y. Luo, Targeting macrophages in cancer immunotherapy. *Signal Transduct. Target. Ther.* **6**, 127 (2021).
16. C. B. Rodell *et al.*, TLR7/8-agonist-loaded nanoparticles promote the polarization of tumour-associated macrophages to enhance cancer immunotherapy. *Nat. Biomed. Eng.* **2**, 578–588 (2018).
17. M. Blachier, H. Leleu, M. Peck-Radosavljevic, D. C. Valla, F. Roudot-Thoraval, The burden of liver disease in Europe: A review of available epidemiological data. *J. Hepatol.* **58**, 593–608 (2013).
18. D. Schuppan, N. H. Afdhal, Liver cirrhosis. *Lancet* **371**, 838–851 (2008).
19. J. M. Llovet *et al.*, Hepatocellular carcinoma. *Nat. Rev. Dis. Primers* **7**, 6 (2021).
20. M. A. Karsdal *et al.*, The good and the bad collagens of fibrosis – Their role in signaling and organ function. *Adv. Drug Deliv. Rev.* **121**, 43–56 (2017).
21. D. Schuppan, Liver fibrosis: Common mechanisms and antifibrotic therapies. *Clin. Res. Hepatol. Gastroenterol.* **39** (suppl. 1), S51–S59 (2015).
22. D. Schuppan, Y. O. Kim, Evolving therapies for liver fibrosis. *J. Clin. Invest.* **123**, 1887–1901 (2013).
23. D. Schuppan, M. Ashfaq-Khan, A. T. Yang, Y. O. Kim, Liver fibrosis: Direct antifibrotic agents and targeted therapies. *Matrix Biol.* **68-69**, 435–451 (2018).
24. S. Van Herck *et al.*, Transiently thermoresponsive acetal polymers for safe and effective administration of amphotericin B as a vaccine adjuvant. *Bioconjug. Chem.* **29**, 748–760 (2018).
25. D. Zhou *et al.*, Anticancer drug disulfiram for in situ RAFT polymerization: Controlled polymerization, multifacet self-assembly, and efficient drug delivery. *ACS Macro Lett.* **5**, 1266–1272 (2016).
26. F. Meraz-Torres, S. Plöger, C. Garbe, H. Niessner, T. Sinnberg, Disulfiram as a therapeutic agent for metastatic malignant melanoma-old myth or new logos? *Cancers (Basel)* **12**, 1–20 (2020).
27. J. S. Barbosa, F. A. Almeida Paz, S. S. Braga, Bisphosphonates, old friends of bones and new trends in clinics. *J. Med. Chem.* **64**, 1260–1282 (2021).
28. K. Ohno, K. Mori, M. Orita, M. Takeuchi, Computational insights into binding of bisphosphates to farnesyl pyrophosphate synthase. *Curr. Med. Chem.* **18**, 220–233 (2011).
29. S. L. Teitelbaum, Bone resorption by osteoclasts. *Science* **289**, 1504–1509 (2000).
30. T. L. Rogers, I. Holen, Tumour macrophages as potential targets of bisphosphonates. *J. Transl. Med.* **9**, 177 (2011).
31. M. Coscia *et al.*, Zoledronic acid repolarizes tumour-associated macrophages and inhibits mammary carcinogenesis by targeting the mevalonate pathway. *J. Cell. Mol. Med.* **14**, 2803–2815 (2010).
32. J. D. Veltman *et al.*, Zoledronic acid impairs myeloid differentiation to tumour-associated macrophages in mesothelioma. *Br. J. Cancer* **103**, 629–641 (2010).
33. A. G. Porras, S. D. Holland, B. J. Gertz, Pharmacokinetics of alendronate. *Clin. Pharmacokinet.* **36**, 315–328 (1999).
34. M. Ovais, M. Guo, C. Chen, Tailoring nanomaterials for targeting tumor-associated macrophages. *Adv. Mater.* **31**, e1808303 (2019).
35. N. Van Rooijen, A. Sanders, Liposome mediated depletion of macrophages: Mechanism of action, preparation of liposomes and applications. *J. Immunol. Methods* **174**, 83–93 (1994).
36. H. D. Danenberg *et al.*, Systemic depletion of macrophages by liposomal bisphosphonates reduces neointimal formation following balloon-injury in the rat carotid artery. *J. Cardiovasc. Pharmacol.* **42**, 671–679 (2003).
37. E. Haber *et al.*, Peritoneal macrophage depletion by liposomal bisphosphonate attenuates endometriosis in the rat model. *Hum. Reprod.* **24**, 398–407 (2009).
38. G. R. Kieczykowski *et al.*, Preparation of (4-amino-1-hydroxybutylidene)bisphosphonic acid sodium salt, MK-217 (alendronate sodium). An improved procedure for the preparation of 1-hydroxy-1,1-bisphosphonic acids. *J. Org. Chem.* **60**, 8310–8312 (1995).
39. J. P. Jansen, G. J. Bergman, J. Huels, M. Olson, Prevention of vertebral fractures in osteoporosis: Mixed treatment comparison of bisphosphonate therapies. *Curr. Med. Res. Opin.* **25**, 1861–1868 (2009).
40. N. Leber, L. Nuhn, R. Zentel, Cationic nanohydrogel particles for therapeutic oligonucleotide delivery. *Macromol. Biosci.* **17**, 1700092 (2017).
41. J. Stickdorn, L. Nuhn, Reactive-ester derived polymer nanogels for cancer immunotherapy. *Eur. Polym. J.* **124**, 109481 (2020).
42. L. Nuhn *et al.*, pH-degradable imidazoquinoline-ligated nanogels for lymph node-focused immune activation. *Proc. Natl. Acad. Sci. U.S.A.* **113**, 8098–8103 (2016).
43. L. Nuhn *et al.*, Nanoparticle-conjugate TLR7/8 agonist localized immunotherapy provokes safe antitumoral responses. *Adv. Mater.* **30**, e1803397 (2018).
44. J. Kockelmann *et al.*, Control over imidazoquinoline immune stimulation by pH-degradable poly(norbornene) nanogels. *Biomacromolecules* **21**, 2246–2257 (2020).
45. L. Nuhn *et al.*, Potent anti-viral vaccine adjuvant based on pH-degradable nanogels with covalently linked small molecule imidazoquinoline TLR7/8 agonist. *Biomaterials* **178**, 643–651 (2018).
46. A. Das, P. Theato, Activated ester containing polymers: Opportunities and challenges for the design of functional macromolecules. *Chem. Rev.* **116**, 1434–1495 (2016).
47. A. Huppertsberg *et al.*, Squaric ester-based, pH-degradable nanogels: Modular nanocarriers for safe, systemic administration of toll-like receptor 7/8 agonistic immune modulators. *J. Am. Chem. Soc.* **143**, 9872–9883 (2021).
48. S. Schmitt *et al.*, Fluorescence correlation spectroscopy monitors the fate of degradable nanocarriers in the blood stream. *Biomacromolecules*, 10.1021/acs.biomac.1c01407 (2021).
49. G. Genard, S. Lucas, C. Michiels, Reprogramming of tumor-associated macrophages with anticancer therapies: Radiotherapy versus chemo- and immunotherapies. *Front. Immunol.* **8**, 828 (2017).
50. V. Rouach *et al.*, Exposure to alendronate is associated with a lower risk of bone metastases in osteoporotic women with early breast cancer. *J. Bone Oncol.* **12**, 91–95 (2018).
51. L. Nuhn *et al.*, FRET monitoring of intracellular ketal hydrolysis in synthetic nanoparticles. *Angew. Chem. Int. Ed. Engl.* **57**, 10760–10764 (2018).
52. K. Rausch, A. Reuter, K. Fischer, M. Schmidt, Evaluation of nanoparticle aggregation in human blood serum. *Biomacromolecules* **11**, 2836–2839 (2010).
53. A. Warnecke, S. Abele, S. Musunuri, J. Bergquist, R. A. Harris, Scavenger receptor A mediates the clearance and immunological screening of MDA-modified antigen by M2-type macrophages. *Neuromolecular Med.* **19**, 463–479 (2017).
54. J. Canton, D. Neculai, S. Grinstein, Scavenger receptors in homeostasis and immunity. *Nat. Rev. Immunol.* **13**, 621–634 (2013).
55. L. Peiser, S. Gordon, The function of scavenger receptors expressed by macrophages and their role in the regulation of inflammation. *Microbes Infect.* **3**, 149–159 (2001).
56. C. Jiménez Calvente *et al.*, Specific hepatic delivery of procollagen α1(I) small interfering RNA in lipid-like nanoparticles resolves liver fibrosis. *Hepatology* **62**, 1285–1297 (2015).

57. Y. Popov *et al.*, Tissue transglutaminase does not affect fibrotic matrix stability or regression of liver fibrosis in mice. *Gastroenterology* **140**, 1642–1652 (2011).
58. N. Leber *et al.*, SiRNA-mediated in vivo gene knockdown by acid-degradable cationic nanohydrogel particles. *J. Control. Release* **248**, 10–23 (2017).
59. L. Kaps *et al.*, In vivo gene-silencing in fibrotic liver by siRNA-loaded cationic nanohydrogel particles. *Adv. Healthc. Mater.* **4**, 2809–2815 (2015).
60. D. Schuppan, Structure of the extracellular matrix in normal and fibrotic liver: Collagens and glycoproteins. *Semin. Liver Dis.* **10**, 1–10 (1990).
61. D. Schuppan, M. Ruehl, R. Somasundaram, E. G. Hahn, Matrix as a modulator of hepatic fibrogenesis. *Semin. Liver Dis.* **21**, 351–372 (2001).
62. Y. O. Kim, Y. Popov, D. Schuppan, Optimized mouse models for liver fibrosis. *Methods Mol. Biol.* **1559**, 279–296 (2017).
63. S. Ma, Y. Dai, Principal component analysis based methods in bioinformatics studies. *Brief. Bioinform.* **12**, 714–722 (2011).
64. F. Foerster *et al.*, Enhanced protection of C57 BL/6 vs Balb/c mice to melanoma liver metastasis is mediated by NK cells. *OncoImmunology* **7**, e1409929 (2017).
65. A. Subramanian *et al.*, Gene set enrichment analysis: A knowledge-based approach for interpreting genome-wide expression profiles. *Proc. Natl. Acad. Sci. U.S.A.* **102**, 15545–15550 (2005).
66. S. M. Zeisberger *et al.*, Clodronate-liposome-mediated depletion of tumour-associated macrophages: A new and highly effective antiangiogenic therapy approach. *Br. J. Cancer* **95**, 272–281 (2006).